Supplementary Information: Accelerated screening of oxide semiconductors by combinatorial spray deposition and high-throughput analysis

Maximilian Wolf*[ab], Georg K. H. Madsen[b] and Theodoros Dimopoulos*[a]

[a] *Energy Conversion and Hydrogen, Center for Energy, AIT Austrian Institute of Technology GmbH, 1210 Vienna, Austria. E-mail: maximilian.wolf@ait.ac.at, theodoros.dimopoulos@ait.ac.at*
[b] *Institute of Materials Chemistry, TU Wien, 1060 Vienna, Austria.*

S1 Pump system

As pictured in Fig. S1, the pump system is designed to simultaneously use the three pumps from the left or the two outer pumps. This enables mixing of precursor solutions as well as switching between deposition of precursor and nanoparticle solutions. The major part of the structural components are produced by rapid prototyping techniques, as depicted in the exploded 3D model in Fig. S2. The realized setup is shown in Fig. S3 with the pumps and the magnetic valves (not visible) mounted on a wooden plate and the electronic parts in the junction box next to it. The graphical user interface (GUI), as depicted in Fig. S4, consist of control boxes for each of the four pumps in the top part, the schematic diagram in the bottom left, which shows the state of the pumps and valves, and the menu in the bottom right, where experiments can be configured, saved, and started. A schematic of the electronics is available as separate image in the ESI (https://doi.org/10.1039/d3ma00136a, *Electronics schematic*) to facilitate the rebuild of the system. The 3D model of the pump and the GUI will be provided upon genuine request to the corresponding author.

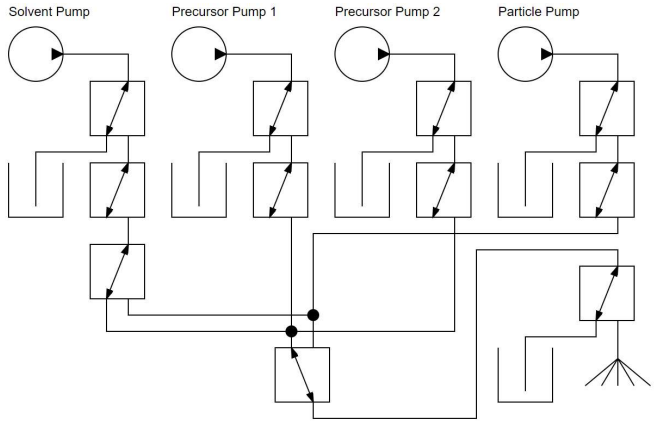

Fig. S1 Schematic diagram of the pump system showing 4 pumps, 5 vessels, 11 magnetic valves and the USP tool.

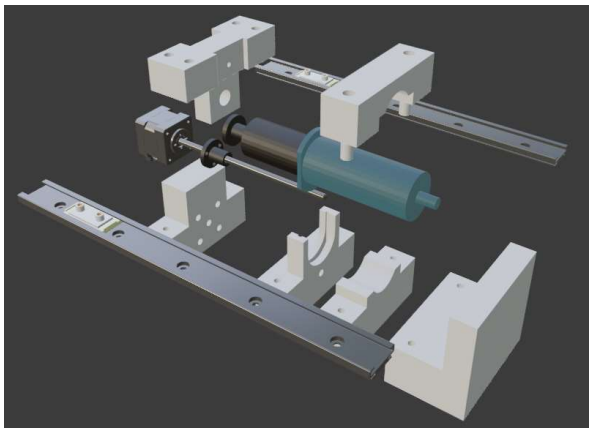

Fig. S2 Exploded 3D model of the pump design, showing the 3D printed structural parts in white.

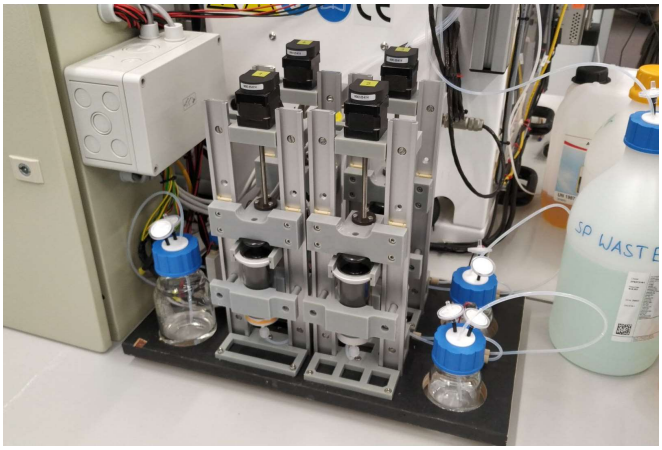

Fig. S3 Photograph of the realized USP pump system.

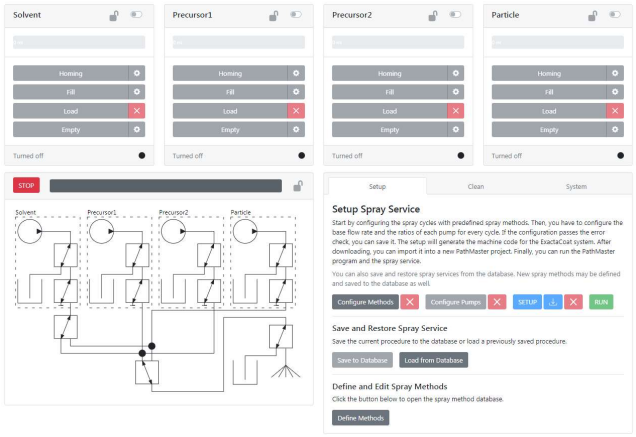

Fig. S4 GUI for the USP pump system.

S2 Combinatorial transmission measurements

Due to the confined available space and the lack of a commercially available solution, a proprietary sample stage for the FTS instrument is designed and built (Fig. S5). It consists of two piezo-motor-driven linear axes which move the sample in horizontal and vertical directions, and 3D-printed structural components. A control software is developed to move the sample stage and perform measurements automatically. The easy-to-use GUI is shown in Fig. S6, exemplarily configured for 15 UV transmission measurements. Since the data is stored in a ready-to-use format, it can be directly loaded into the evaluation script (Python Jupyter Notebook) which includes widgets for interactive examination of the analysis results, e.g. Fig. S7. The 3D model of the sample holder will be provided upon genuine request to the corresponding author.

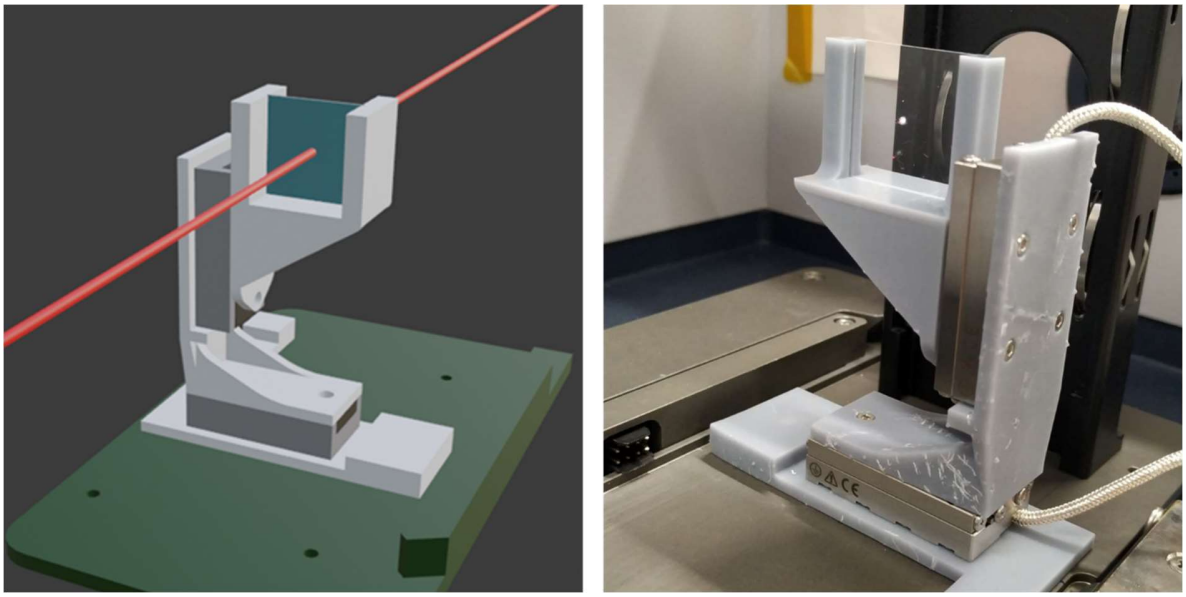

Fig. S5 3D model of the FTIR sample stage (left) and the realized system (right).

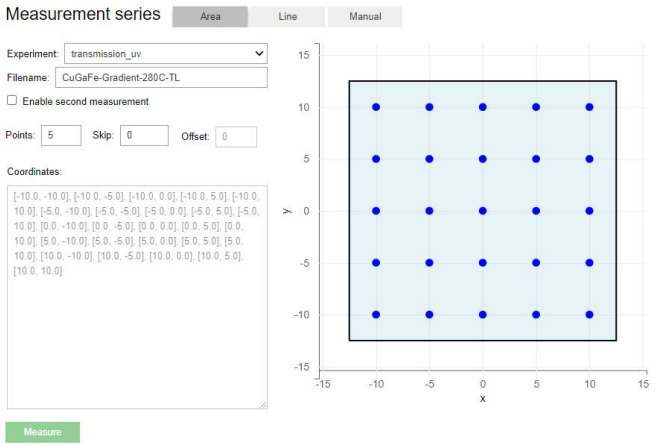

Fig. S6 GUI for the (semi-)automatized FTS measurements.

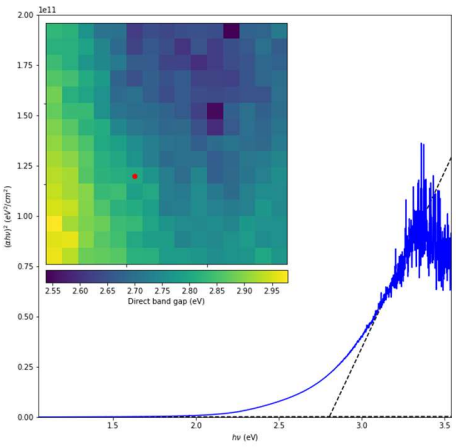

Fig. S7 Interactive Tauc plot from transmission measurements of a combinatorial deposit.

S3 Combinatorial X-ray diffraction

A similar approach to the FTS setup is followed for upgrading the XRD instrument. This time, the stage consists of a rotation axis instead of a second linear axis which is necessary to reach the entire sample space. Additionally, a brass tube is added for confining the X-ray beam in a small, circular shape (Fig. S8). The FTS control software and GUI is mostly repurposed but is reconfigured to work with the rotation axis and the XRD measurement software. The data evaluation is also based on Python Jupyter Notebooks enabling interactive exploration of the measurements and comparison with reference diffraction pattern. The 3D model of the sample holder will be provided upon genuine request to the corresponding author.

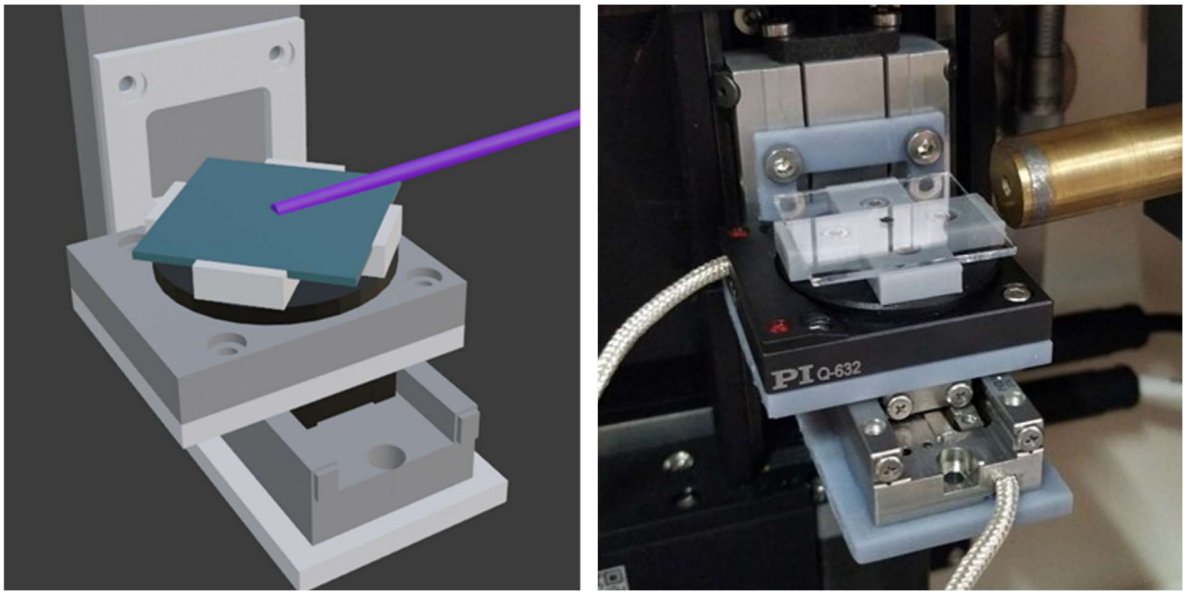

Fig. S8 3D model of the XRD sample stage (left) and the realized system (right).

S4 Stability of band gap

The band gap of the same combinatorial film is evaluated a second time after leaving it under ambient conditions for over 5 months (11.11.2022–18.04.2023). Exactly the same procedure as described in text (Results and discussion, Optical properties) is used which yields maps of direct and indirect band gap values (Fig. S9). These are used to calculate the relative deviations from the same pixels of the previously obtained data like the calculation of the compositional reproducibility in the main text (Results and discussion, Composition). This leads to average errors for the direct and indirect band gap of 1.43 % and 1.82 %, respectively (Fig. S10). Since the errors are comparable to the general band gap reproducibility (S28), the films can be considered stable with respect to the evaluated band gap energies.

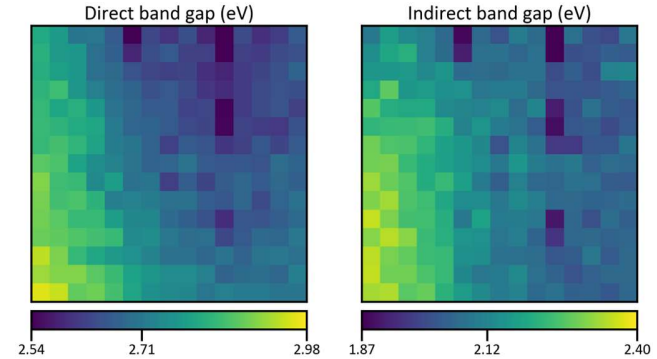

Fig. S9 Maps of direct and indirect band gaps evaluated using the Tauc method of a combinatorial film which was kept under ambient conditions for over 5 months The values of the colour bars are the minimum, the mean, and the maximum band gap energy.

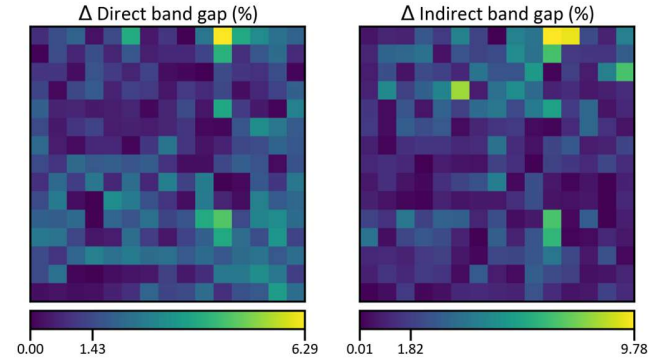

Fig. S10 Maps of relative deviation of the direct and indirect band gap before and after it was kept under ambient conditions for over 5 months. The values of the colour bar are the minimum, the mean, and the maximum relative deviation.

S5 SDD model for NIST DTSA-II

Since the employed Monte Carlo simulation software, NIST DTSA-II,[1,2] relies heavily on an accurate definition of the detector model, the parameters in Table S1 are carefully collected from the meta data of measurement files and online resources.[3,4]

Table S1 SDD model parameters for NIST DTSA-II.

Window	**Elevation angle**	**Azimuthal angle**	**Optimal working distance**
Amptek C2 Si_3N_4	35.0 °	0.0 °	8.5 mm
Sample-to-detector distance	**Detector area**	**Gold layer**	**Aluminium layer**
30.0 mm	30.0 mm^2	0.0 nm	10.0 nm
Nickel layer	**Dead layer**	**Thickness**	**Number of channels**
0.0 nm	0.03 µm	1.0 mm	4096
Zero strobe discriminator	**Energy scale**	**Zero offset**	**Resolution**
0.0 eV	10.0 eV/channel	0.0 eV	127.5 eV FWHM at Mn Kα

S6 Soda-lime glass properties

The specific gravity of 2.479 and the chemical composition in Table S2 are taken from [5].

Table S2 Chemical composition of Thermo Scientific extra-white glass in wt%. The components in red are not used for the Monte Carlo simulations.

SiO_2	MgO	Na_2O	Al_2O_3	K_2O	Fe_2O_3	CaO	SO_3
72.20	4.30	14.30	1.20	1.20	0.03	6.40	0.30

S7 eZAF correction factors

The heavy elements Cu, Ga, and Fe are, as expected, much less affected by absorption losses than the lighter elements (Table S3). Hence, the quantification should yield acceptable results after normalization, especially because A is almost equal for the three elements.

Table S3 Correction factors of the standardless eZAF quantification of the as-deposited film averaged over all 225 pixels plus/minus the standard deviation. Z, A, and F are the atomic number, absorption, and fluorescence effects, respectively.

Element	**Z**	**A**	**F**
O	0.858 ± 0.003	0.190 ± 0.006	1.000 ± 0.000
Na	0.875 ± 0.003	0.180 ± 0.014	1.003 ± 0.000
Mg	0.880 ± 0.003	0.195 ± 0.006	1.003 ± 0.000
Al	0.885 ± 0.003	0.284 ± 0.011	1.005 ± 0.001
Si	0.889 ± 0.002	0.398 ± 0.012	1.005 ± 0.000
K	0.911 ± 0.002	0.813 ± 0.003	1.037 ± 0.002
Ca	0.914 ± 0.002	0.855 ± 0.003	1.046 ± 0.003
Fe	0.937 ± 0.002	0.967 ± 0.001	1.148 ± 0.020
Cu	0.949 ± 0.001	0.971 ± 0.003	1.157 ± 0.035
Ga	0.957 ± 0.001	0.969 ± 0.004	1.069 ± 0.002

S8 ZAF Quantification of Monte Carlo simulations

The Monte Carlo (MC) simulation spectra for the thickness estimation of the as-deposited film are quantified using the built-in ZAF quantification algorithm of NIST DTSA-II "ZAF-style". To this end, standard spectra of pure elements are obtained from MC simulations, employing the same SDD model. The results are normalized to Cu, Ga, and Fe as described in the main text (Results and discussion, Composition) and the minimum, mean, and maximum values are plotted against the thickness of the simulated film in Fig. S11. As indicated with the red dashed line at 600 nm, the molar fractions x of the investigated films are within 10 % of the "bulk" molar fraction at 1500 nm x_{1500}. It must be pointed out that the "ZAF-style" algorithm is very basic and the accuracy of the APEX™ eZAF algorithm is expected to be better.

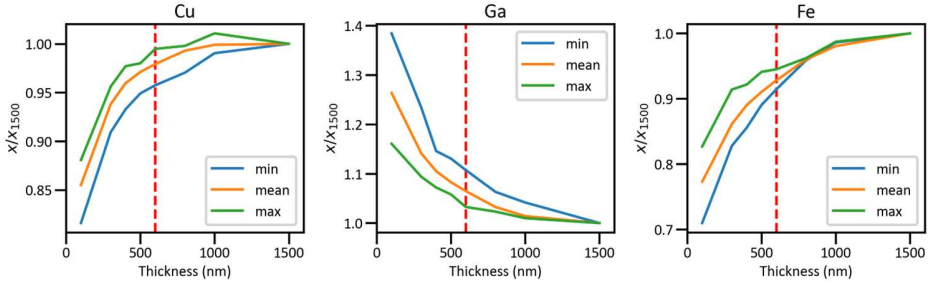

Fig. S11 Minimum, mean, and maximum molar fractions relative to the molar fraction at 1500 nm film thickness of MC simulated spectra. The NIST DTSA-II "ZAF-style" algorithm was employed for the quantification.

S9 Simulation of concentration maps

The combinatorial deposition experiment as described in the main text (Experimental, Sample preparation) is simulated using a basic Python script which does not take into account any forces acting on the droplets (as in [6], e.g.), the sticking coefficients of the pyrolyzed precursor solutions, or the extent of the spray cone. It simply calculates pixel for pixel the current composition of the precursor solution. The following code is annotated with brief descriptions of what it does. The first part results in the vertical and horizontal gradients as depicted in Fig. S12, which represent the fraction of the gradient in % for each mm^2. Afterwards, the elemental concentrations are incorporated and the arrays are combined. This leads to the normalized concentration maps in Fig. S13 which feature the same non-uniform vertical and horizontal gradients of Ga and Fe, respectively, as described in the main text (Results and discussion, Composition). In comparison to the realized experiment, the effect is much less pronounced and the concentration spread is much higher. However, this most probably is related to the neglected effects mentioned above.

```
import numpy as np

## generate vertical and horizontal gradients as numpy arrays

# conversion factor between arb. length unit of USP tool to mm (200 = 1 mm)
cf = 200

# the size of the sprayed area is 22000 in x-direction and 19000 in y-direction, i.e. 110x95 mm
vx = 22000 / cf
hy = 19000 / cf

# this corresponds to 25 horizontal lines for the vertical gradient
# and 27 vertical lines for the horizontal gradient
vdy = 760 / cf
vny = 25
hdx = 815 / cf
hnx = 27

# the numpy arrays are initialized with the correct shape and filled with 1
vertical = np.ones((int(vdy * vny), int(vx)))
horizontal = np.ones((int(hdx * hnx), int(hy)))

# concentrations of the vertical and horizontal lines in % are computed
vlines = np.vstack(
    [np.linspace(100 - i * 100/vny, 100 - (i+1) * 100/vny, vertical.shape[1]) for i in range(vny)]
)
hlines = np.vstack(
    [np.linspace(100 - i * 100/hnx, 100 - (i+1) * 100/hnx, horizontal.shape[1]) for i in range(hnx)
])

# the lines are mapped onto the arrays
# since the spray nozzle goes back and forth, every second gradient line is flipped
for i in range(vny):
    vgradient = vlines[i]
    if i%2:
        vgradient = np.flip(vgradient)
    vertical[int(i*vdy):int((i+1)*vdy)] = vertical[int(i*vdy):int((i+1)*vdy)] * vgradient
for i in range(hnx):
    hgradient = hlines[i]
    if not i%2:
        hgradient = np.flip(hgradient)
    horizontal[int(i*hdx):int((i+1)*hdx)] = horizontal[int(i*hdx):int((i+1)*hdx)] * hgradient

# the horizontal gradient is rotated
horizontal = np.rot90(horizontal, 1)
```

```
## incorporate elemental information

# precursor solution concentrations in mmol/l
cu = 25
ga = 40
fe = 30

# cu is sprayed twice, vertically and horizontally
# ga and fe gradients are subtracted from 100% because they go in the reverse direction
# the gradients are multiplied by the number of spray cycles but this factor will cancel out
cu_gradient = 20 * (vertical + horizontal) * cu
ga_gradient = 20 * (100 - vertical) * ga
fe_gradient = 20 * (100 - horizontal) * fe

# the gradients are stacked and normalized
stacked_gradients = np.stack([cu_gradient, ga_gradient, fe_gradient])
normalized_gradients = stacked_gradients / stacked_gradients.sum(axis=0)

# the arrays are cropped to the center of the sprayed area to reflect the size of the 3x3 substrates
# i.e. 75x75 mm
cropped_gradients = stacked_gradients[:,10:-10,18:-17]
normalized_cropped_gradients = cropped_gradients / cropped_gradients.sum(axis=0)
```

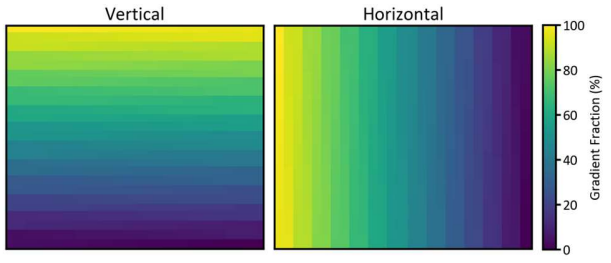

Fig. S12 Calculated gradients of 25 vertical and 27 horizontal lines on a 110x95 mm area.

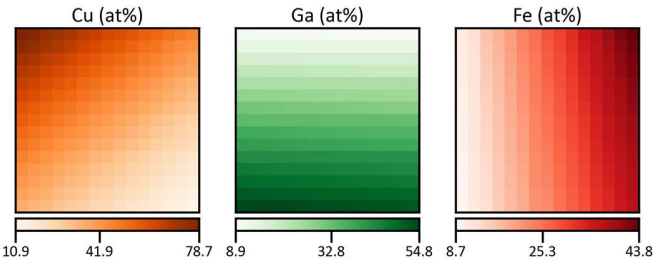

Fig. S13 Normalized concentration maps of the simulated combinatorial spray deposition. The values of the colour bar are the minimum, the mean, and the maximum mole fraction.

S10 Compositional spread of data

Fig. S13 and Fig. S14 depict the data points in binary plots and a ternary diagram, respectively.

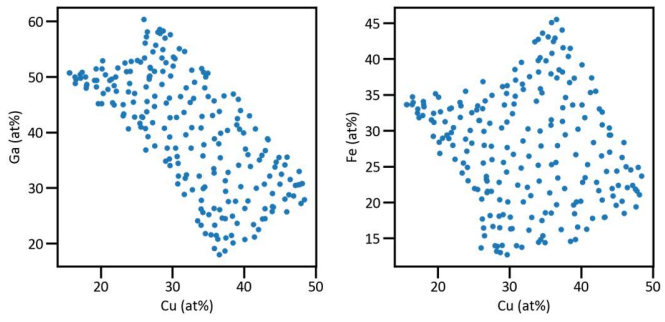

Fig. S14 Binary composition plots.

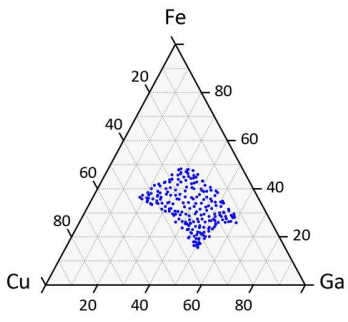

Fig. S15 Ternary composition diagram.

S11 Reproducibility of the combinatorial deposition

An additional combinatorial film is deposited and analysed by EDS measurements as described in the main text (Results and discussion, Composition). This results in the composition maps of Fig. S16 which feature three vertical lines of missing data. Chronologically, this film was deposited earlier than the data that is shown in the main text and was later used for the heat treatment. The EDS measurement routine was not ideal yet and did not exactly move to the correct positions. Part of the reproducibility error can be attributed to these positional errors. However, the data was mainly removed because the measurement area partially overlapped with conductive copper tape which was not used in later measurements. Still, the remaining pixels should be comparable and are used to calculate the relative deviations as described in the main text, yielding Fig. S17.

S12 Change of composition through heat treatment

The Cu, Ga, and Fe concentration maps of one combinatorial film before and after the annealing heat treatment are compared in the same way as in S12. This results in the maps of relative deviations in Fig. S18.

S13 Oxygen maps

Fig. S19 depicts the non-normalized oxygen concentration maps of the films A and B before and after annealing. The trend of an increasing concentration from top-left to bottom-right is unchanged through the heat treatment. It seems like the annealing would introduce more noise to the data, but this can be attributed to a reduced spread of the values (4.8 vs. 8.2/11.0 at%). The reproducibility of the oxygen concentration (3.2 %) is similar to the reproducibility of Cu, Ga, and Fe (S11).

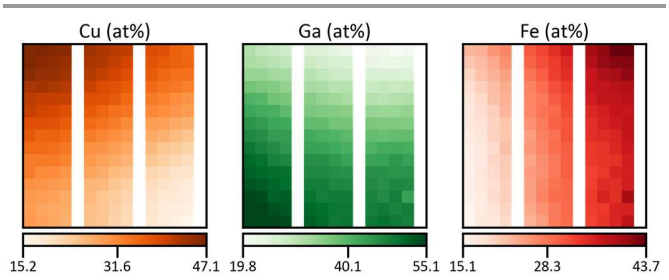

Fig. S16 Normalized mole fraction maps of the elemental gradients obtained by EDS measurements with standardless quantification of an additional combinatorial film. The white vertical lines are missing data which originate from imperfect measurement conditions (see text). The values of the colour bar are the minimum, the mean, and the maximum mole fraction.

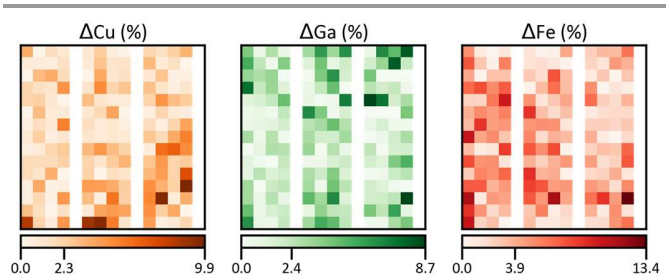

Fig. S17 Maps of relative deviation of the Cu, Ga, and Fe concentration maps of two equally prepared combinatorial films. The white vertical lines are missing data which originate from imperfect measurement conditions (see text). The values of the colour bar are the minimum, the mean, and the maximum relative deviation.

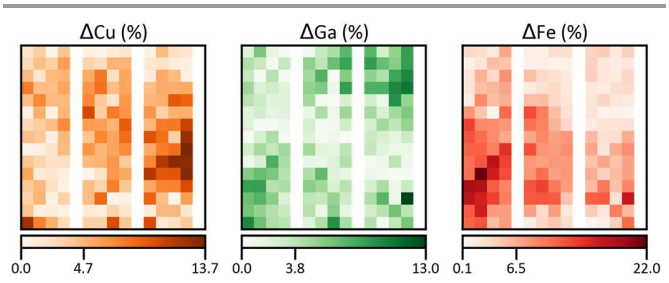

Fig. S18 Maps of relative deviation of the Cu, Ga, and Fe concentration maps of one combinatorial film before and after the annealing heat treatment. The white vertical lines are missing data which originate from imperfect measurement conditions (see text). The values of the colour bar are the minimum, the mean, and the maximum relative deviation.

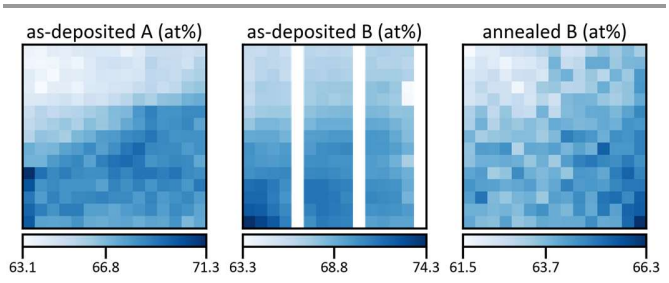

Fig. S19 Non-normalized oxygen mole fraction maps of two equally prepared films (A and B), twice as-deposited and once after the annealing heat treatment. The white vertical lines in “as-deposited B” are missing data which originate from imperfect measurement conditions (see text). The values of the colour bars are the minimum, the mean, and the maximum mole fraction.

S14 Evaluation of sigma for the Gaussian filter

The XRD measurements are smoothened by applying a Gaussian filter which requires the parameter sigma as standard deviation for the Gaussian kernel. To this end, an arbitrary measurement with a prominent peak at 36° is selected and the contribution of the substrate is removed, as described in the main text (Results and discussion, Crystal structure). Then, the measurement is max-normalized and plotted together with a gaussian function which has an amplitude of 1.0:

```
# define the Gaussian function
# x0...location of the peak maximum
# A...amplitude of the peak
# sigma...standard deviation of the Gaussian distribution
def gauss(x, x0, A=1.0, sigma):
    return A * np.exp(-(x - x0) ** 2 / (2 * sigma ** 2))
```

The location of the peak maximum and the standard deviation are graphically adjusted to fit the data (Fig. S20). The obtained sigma should be a good approximation for the average peak width and can be used to smoothen the data in order to facilitate the further analysis.

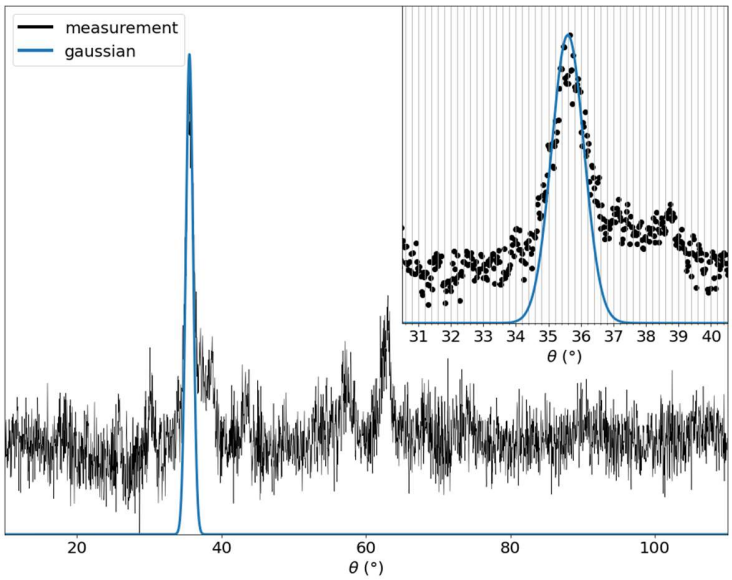

Fig. S20 Graphical evaluation of the peak width for the Gaussian filter.

S15 Composition dependence of the 36° peak prominence (as-deposited film)

The prominence of the peak at 36° is obtained by subtracting the mean of the XRD measurements from the height of the peak. Beforehand, the data is minmax-normalized in order to obtain comparable results. After resizing the composition maps to a size of 12x12 pixels (0), each peak prominence is plotted against the Cu, Ga, and Fe concentration of the respective pixel. The invalid measurements in the corners of each substrate are omitted. Fig. S21 depicts the results of the evaluation which features two lines, one solid and one dashed which are obtained from linear and quadratic regression, respectively.

S16 Composition dependence of the 36° peak prominence (annealed film)

The measurements of the annealed film are treated the same as in S15 which results in Fig. S22.

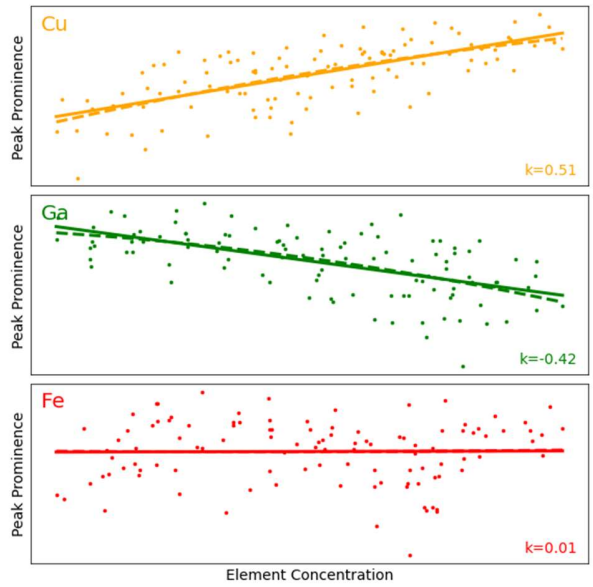

Fig. S21 Composition dependence of the 36° peak prominence from minmax-normalized XRD measurements of the as-deposited film. One solid and one dashed line is displayed, representing the linear and quadratic regression, respectively. The slope of the linear regression is shown in the bottom right.

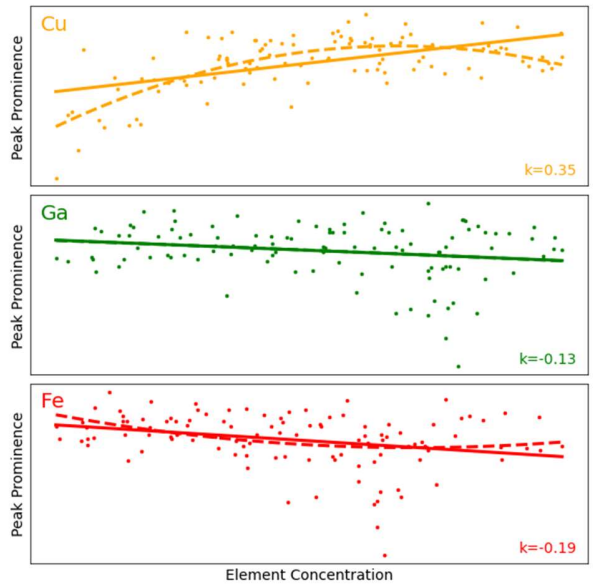

Fig. S22 Composition dependence of the 36° peak prominence from minmax-normalized XRD measurements of the annealed film. One solid and one dashed line is displayed, representing the linear and quadratic regression, respectively. The slope of the linear regression is shown in the bottom right.

S17 Fit results of the crystal structure evaluation

Fig. S23 depicts some meta data results from the XRD curve fitting as described in the main text (Results and discussion, Crystal structure). The root mean squared error (RMSE) is formed between the model curve $\sum F_{SG}^{fit}(\theta)$ and the measurements $F^{meas}(\theta)$ by calculating

$$RMSE = \sqrt{\frac{\sum\left(\sum F_{SG}^{fit}(\theta) - F^{meas}(\theta)\right)^2}{N}}$$

where the outer sum is over all θ angles and N is the number of data points. The maximum of the fit curve can be below 100 % if the measured reflection at 36° is at a different angle than the delafossite maximum, assuming that the excess intensity does not originate from texture. A maximum above 100 % indicates texture of the spinel structure because the heights of the reflections at 30° and 57° do not fit the reference pattern; other crystal structures which diffract at these angles are also possible. The background factor is the height of the max-normalized measurement at the position of the background maximum, i.e., calculated like this:

```
bg_maxpos = background.argmax() # numpy argmax finds the index of the maximum of an iterable
bg_factor = max_normalization(measurement)[bg_maxpos-10:bg_maxpos+10].mean() # averaging +/-10 data points
```

S18 Up-/downsampling a property map

In order to change the resolution of a property map, the initial matrix is inflated by repeating each pixel several times such that the number of pixels in both axes (i.e., width and height) is the least common denominator (LCD) between the initial and the target widths/heights. The LCD is divided by the target width/height to obtain the size of the pixel window from which the mean gives the value of the corresponding pixel in the target resolution. E.g., in order to reduce from 5×5 pixels to 4×4 pixels, the matrix is inflated to 20×20 pixels. Then, the window size is found to be 20/4×20/4 = 5×5 pixels and the mean of all 16 windows is formed (Fig. S24). The same procedure is followed to upsample a property map in S20.

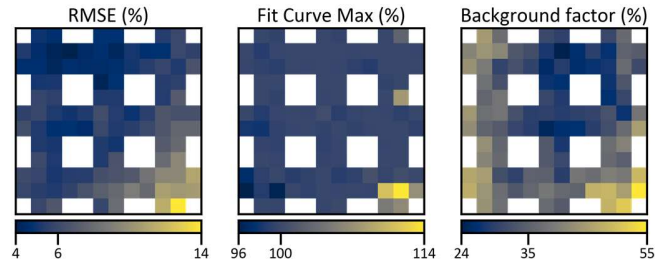

Fig. S23 From left to right: root mean squared error between XRD fit and measurement, maximum of the XRD fit (optimum: 100 %), and factor of the removed background for the data pre-processing. The values of the colour bars are the minimum, the mean, and the maximum percentage.

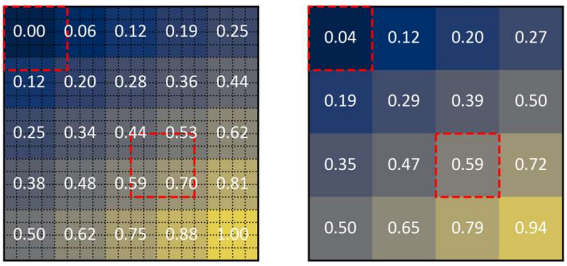

Fig. S24 Example of downsampling the resolution of a property map from 5×5 pixels to 4×4 pixels. The mean of the small squares inside each red dashed square in the left image is the value of the corresponding pixel in the right image.

S19 Composition from crystal structures

The model which correlates the measured EDS composition maps of the combinatorial film with the crystal structures, as presented in the main text (Results and discussion, Crystal structure), is used to obtain the deduced model composition maps in Fig. S25. If delafossite is not considered in the crystal structure evaluation, the resulting composition maps change slightly (Fig. S26) but the composition maps which are based on the intensities from the exhaustive search still agree best with the experimental results.

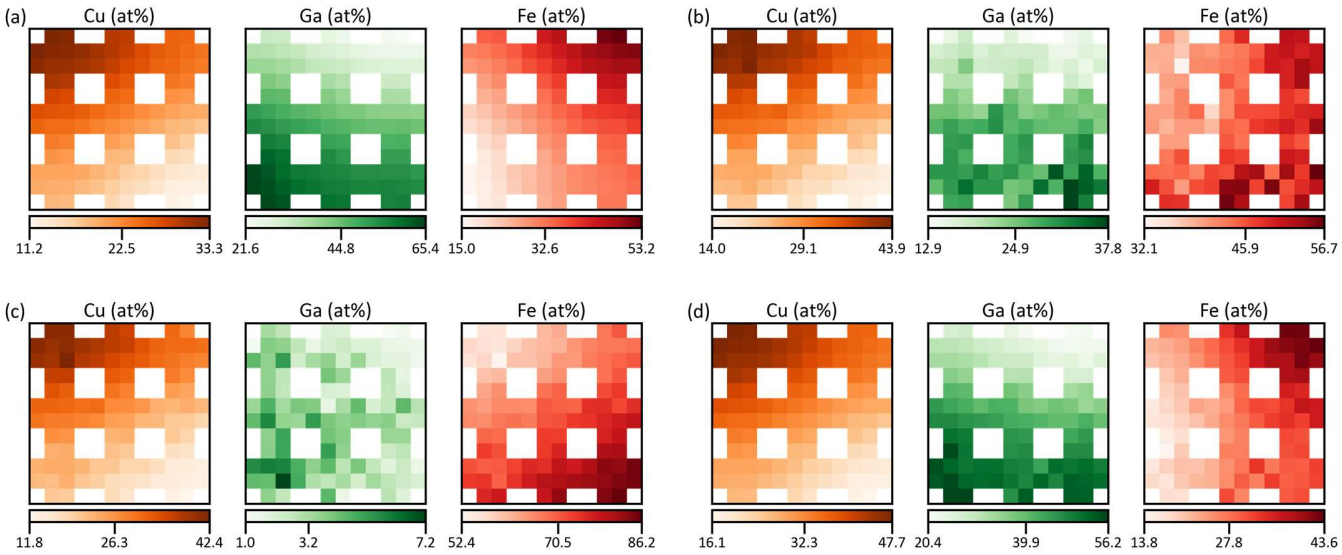

Fig. S25 Composition maps deduced from the initial crystal structures where all compounds are considered using different approaches: (a) only spinel structure with Cu and Ga mole fractions limited to 1/3 and 2/3, respectively, (b) based on normalized intensities, (c) based on absolute intensities, and (d) after optimizing the intensities with the exhaustive search. The values of the colour bars are the minimum, the mean, and the maximum mole fraction.

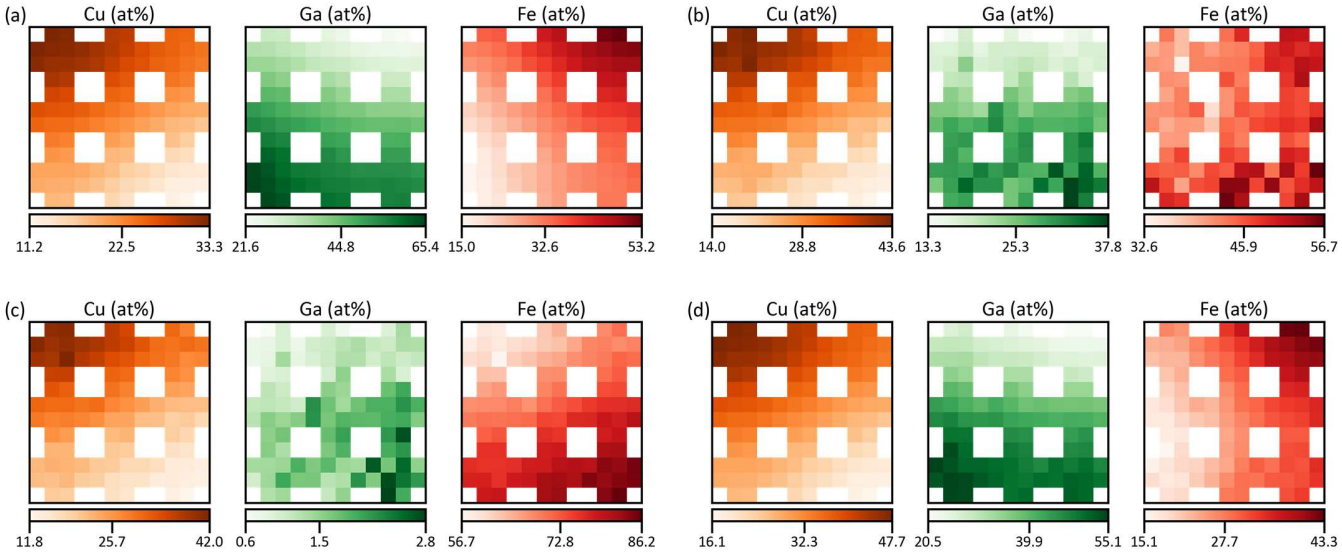

Fig. S26 Composition maps deduced from the crystal structures without considering delafossite using different approaches: (a) only spinel structure with Cu and Ga mole fractions limited to 1/3 and 2/3, respectively, (b) based on normalized intensities, (c) based on absolute intensities, and (d) after optimizing the intensities with the exhaustive search. The values of the colour bars are the minimum, the mean, and the maximum mole fraction.

S20 Filling and upsampling a property map

As exemplarily depicted in Fig. S27, the missing values of the structure maps are filled by the mean values of the surrounding neighbours iteratively. Since the initially empty positions become new neighbours for other positions after the first iteration, a new mean must be formed several times until the values do not change anymore. Afterwards, the resolution is increased from 12×12 pixels to 15×15 pixels as described in S200.

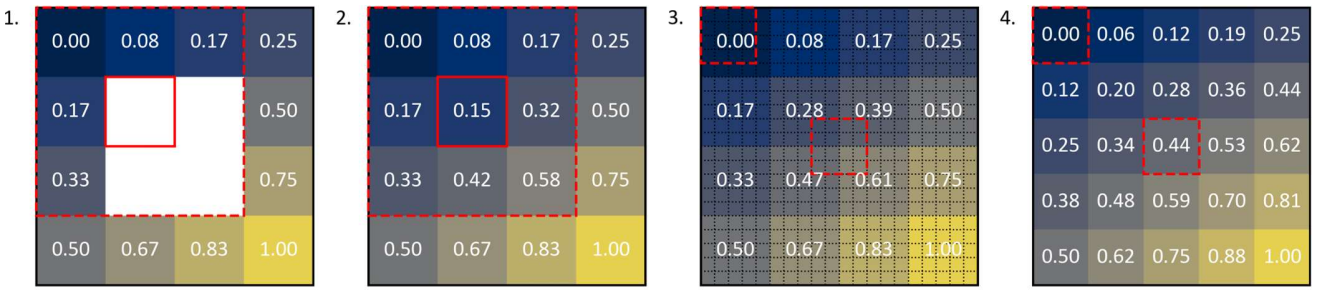

Fig. S27 Procedure of transforming the structure maps from 12×12 pixels with missing positions to complete 15×15 pixels. The image shows a subsection of a data map and uses dummy values for explanatory reasons.

S21 Density from composition and crystal structures

Four methods of computing the density from the composition and crystal structure maps are compared:

```
def compute_density_mean(xis, xims, rhos):
    rhos = np.array(rhos)
    return rhos.mean()

def compute_density_mean_deviation(xis, xims, rhos):
    xis = np.array(xis)
    xims = np.array(xims)
    rhos = np.array(rhos)
    return (rhos.mean() - (rhos.mean() - rhos) * (xims * xis).sum(1)).mean()

def compute_density_linalg(xis, xims, rhos):
    xis = np.array(xis)
    xims = np.array(xims).T
    rhos = np.array(rhos)
    a = np.vstack([xims, np.ones(xims.shape[1])])
    b = np.hstack([xis, 1])
    linsol = np.linalg.lstsq(a, b, rcond=None)[0]
    return np.sum(rhos * linsol)

def compute_density_linprog(xis, xims, rhos):
    xims = np.array(xims).T
    xis = np.array(xis)
    rhos = np.array(rhos)
    G = -np.eye(xims.shape[1])
    h = np.zeros(xims.shape[1])
    A = np.ones(xims.shape[1])
    b = np.ones(1)
    sol = qpsolvers.solve_ls(R=xims, s=xis, G=G, h=h, A=A, b=b, solver='cvxopt')
    return (sol * rhos).sum()
```

`xims` and `rhos` are lists of the compositions and the densities of the considered compounds, respectively. Around 16,000 combinations of the compounds are generated, each described by the overall composition `xis`, the crystal structure amounts, and the true densities. The densities are evaluated as described in the main text (Results and discussion, Thickness) and plotted against the true values in Fig. S28. “Mean Deviation” lowers the root mean squared error (RMSE) and the maximum error (MAXE) slightly in comparison to the trivial “Mean” solution. But the deployed “Linprog” yields a far better agreement between true and predicted densities. Without the constraints, the method does not work, as implemented in “Linalg”.

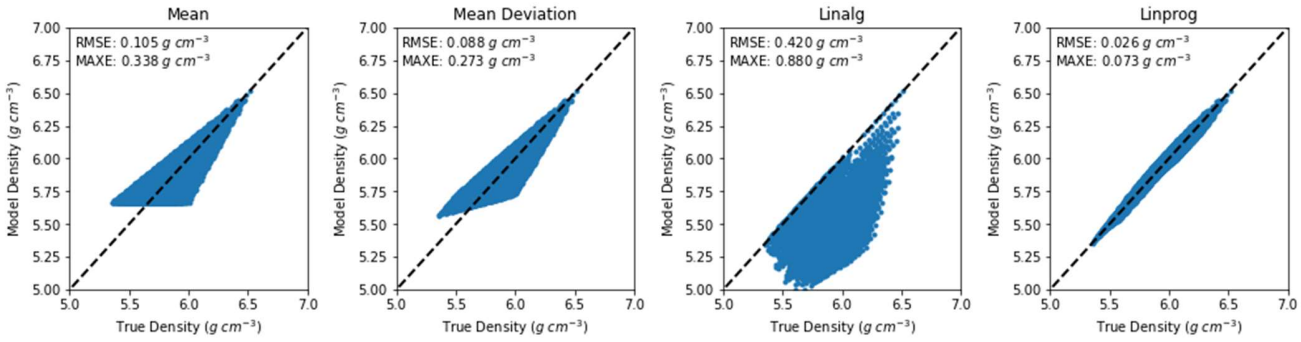

Fig. S28 Predicted versus true densities of 16,000 composition-structure pairs using four different evaluation functions.

S22 RMSE maps of thickness estimation

The root mean squared error (RMSE) between the measured and Monte Carlo (MC) simulated spectra is calculated with

$$RMSE = \sqrt{\frac{\sum\left(I^{meas}(E) - I^{MC}(E)\right)^2}{N}}$$

where I is the intensity of the spectra, E is the energy channel, and N is the total number of channels. This calculation yields the RMSE maps in Fig. S29 which all are similar on average and below 2 %.

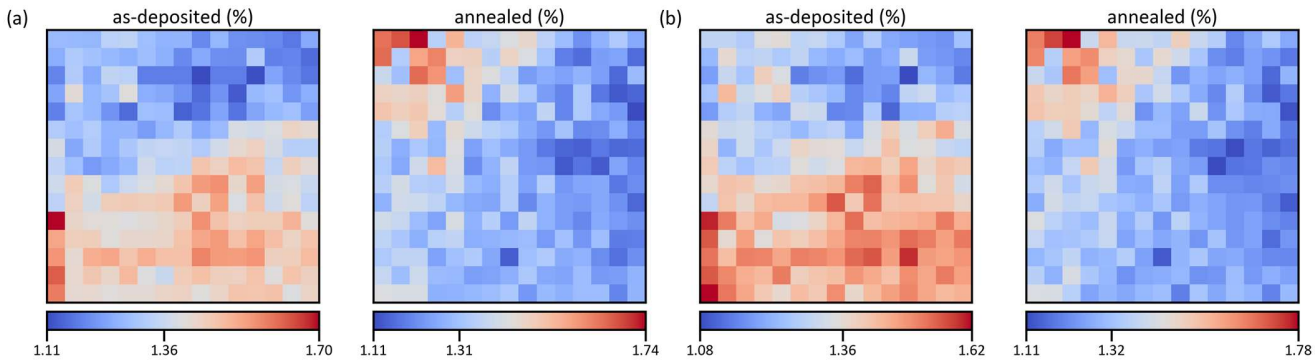

Fig. S29 RMSE maps of the as-deposited and annealed films, calculated based on the structure maps (a) with and (b) without considering delafossite in the evaluation. The values of the colour bars are the minimum, the mean, and the maximum RMSE.

S23 Simulation of thickness distribution

The data from S9 is used to calculate the thickness simply based on the total molar amount:

```
molar_total = stacked_gradients.sum(axis=0)[10:-10,18:-17]
# minmax-normalize the data
molar_total_norm = minmax_normalization(molar_total)
# apply the distribution of the experimental thickness
thickness = molar_total_norm * (700 - 400) + 400
```

This yields the distribution in Fig. S30 which is monotonically increasing from approx. top left to bottom right. This indicates that further factors – mainly the ones that are mentioned in S9 – influence the thickness, especially in the center of the combinatorial area.

S24 Thickness from profilometer measurements

The same combinatorial Cu-Ga-Fe film as before is deposited on another batch of 3×3 glass substrates which are partially covered with a steel mask during the deposition. This yields 9 samples which each are probed using a tactile profilometer on 9 positions for 3 times as depicted in Fig. S31. The mean and the standard deviation of the three measurements are formed which yield the thickness map in Fig. S32. The average thickness and the distribution coincide well with the results from the EDS thickness evaluation in the main text (Results and discussion, Thickness). Only the data range is much higher, but this can be attributed to the high variance of the profilometer measurements. The standard deviation of the three measurements on each of the 9×9 pixels is in an interval of [10, 463] nm and 135 nm on average.

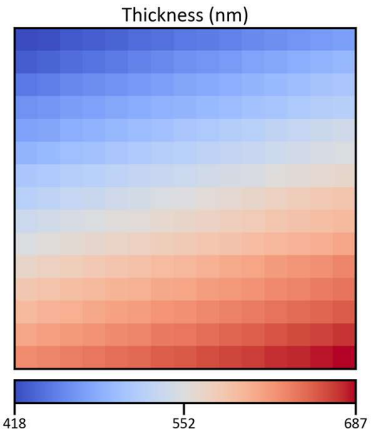

Fig. S30 Simulated thickness distribution based on the data from S9. The values of the colour bars are the minimum, the mean, and the maximum thickness.

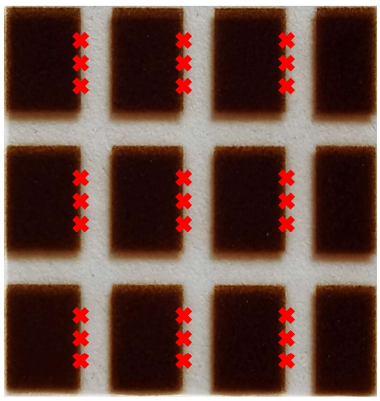

Fig. S31 Photograph of one glass substrate with one section of the combinatorial Cu-Ga-Fe film on it. The sample is partially covered with a steel mask during the deposition, leaving a grid of uncovered glass. Profilometer measurements are conducted on the marked positions.

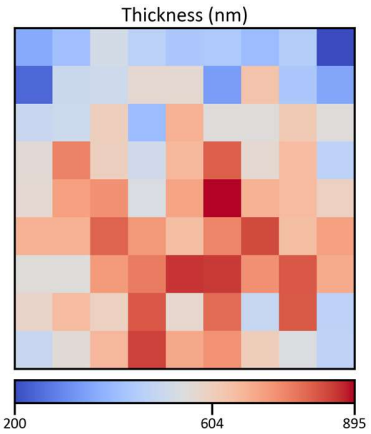

Fig. S32 Thickness distribution from profilometer measurements. The values of the colour bars are the minimum, the mean, and the maximum thickness.

S25 Merging of UV and VIS spectra

The UV and VIS spectra are merged by forming a weighted mean using a sigmoid function in an interval of [-5, 5] where the two spectral regions overlap:

```
import numpy as np

def sigmoid(x):
    return 1 / (1 + np.exp(-x))

# uv and vis are numpy arrays with a shape [2, N], where N is the number of data points
# the wavelength is in the first row
def merge_spectra(uv, vis):
    overlap = np.intersect2d(uv[0], vis[0])
    gradient = sigmoid(np.linspace(-5, 5, len(overlap)))
    return np.hstack([
        uv[:,:-len(overlap)],
        np.vstack([
            overlap,
            (1-gradient)*uv[1][-len(overlap):] + gradient*vis[1][:len(overlap)]
        ]),
        vis[:,len(overlap):]
    ])
```

S26 Reflectance measurements

The reflectance measurements of the as-deposited combinatorial film are depicted in Fig. S33. With the locations of the measurements in the top right of the figure, a tendency of increasing reflectance of the main peak between 500 and 750 nm from top left to bottom right is apparent.

S27 Urbach energy

The Urbach energy E_0 is obtained using the relationship[7]

$$\alpha = \alpha_0 \exp\left(\frac{h\nu - E_1}{E_0}\right)$$

by plotting $\ln(\alpha)$ against $h\nu$ and graphically determining the slope of the exponentially dependent part. This yields the inverse of the Urbach energy which can be used as measure of disorder. Similar to the bandgap evaluation in the main text (Results and discussion, Optical Properties), an automatized routine sequentially calculates linear regressions of $\ln(\alpha)$ with a window size of 89.6 meV in steps of 4.2 meV. From this data, the line with the highest slope is picked to calculate E_0 (Fig. S34 a–b). In the case of the annealed film, the evaluation range is restricted to photon energies above 1.9 eV which prevents that the exponential part of a secondary photon transition is picked (Fig. S34 b). This results in the Urbach energy maps in Fig. S34 c–d, which do not change significantly in the upper two rows of samples (note the different scale of the colour bar) but are significantly different in the bottom row.

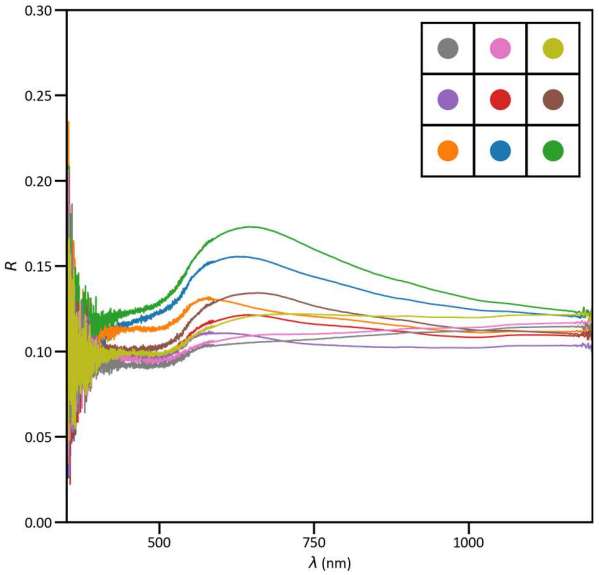

Fig. S33 Reflectance measurements of the combinatorial film, one for each substrate. The locations of the measurements are visualized in the top right.

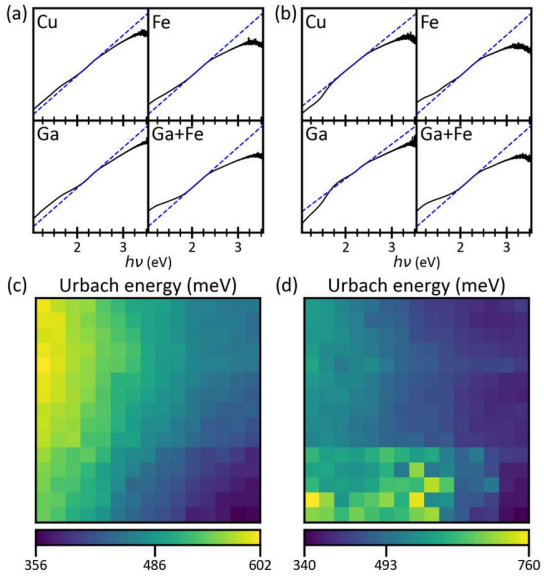

Fig. S34 (a,b) Plots for the evaluation of the Urbach energy of pixels in the Cu, Ga, Fe, and Ga+Fe regions, i.e., top-left, bottom-left, top-right, and bottom-right of the combinatorial film, respectively. (c,d) Resulting Urbach energy maps, where the values of the colour bars are the minimum, the mean, and the maximum Urbach energy. (a,c) and (b,d) are for the as-deposited and for the annealed film, respectively.

S28 Reproducibility of the band gap

An additional combinatorial film is deposited and analysed by FT transmission measurements as described in the main text (Experimental, Sample preparation; Results and discussion, Optical properties). This results in the band gap maps of Fig. S35 which feature three horizontal lines of darker data points, i.e., lower band gap values. Chronologically, this film was deposited earlier than the data that is shown in the main text and was later used for the heat treatment. The FT transmission measurement routine was not ideal yet and the top row of each sample was partially shadowed which resulted in non-correct results. Still, the remaining pixels should be comparable and are used to calculate the relative deviations as described in the main text (Results and discussion, Composition), yielding Fig. S36.

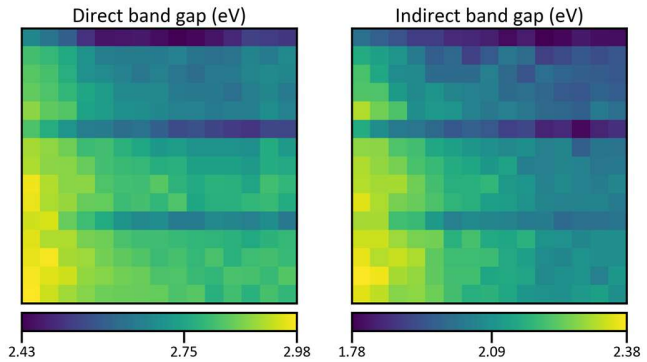

Fig. S35 Maps of direct and indirect band gaps evaluated using the Tauc method of an additional combinatorial film. The darker horizontal lines are erroneous data which originate from imperfect measurement conditions (see text). The values of the colour bars are the minimum, the mean, and the maximum band gap energy.

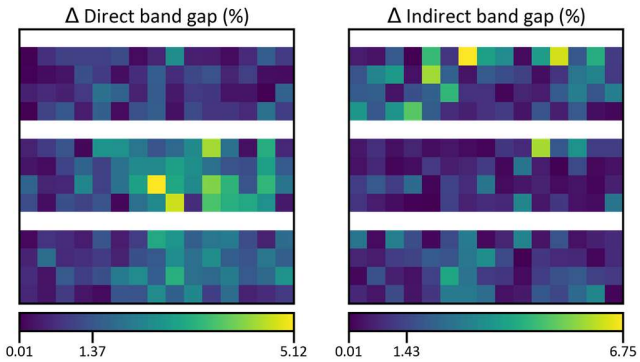

Fig. S36 Maps of relative deviation of the direct and indirect band gap of two equally prepared combinatorial films. The white horizontal lines are removed data which originate from imperfect measurement conditions (see text). The values of the colour bar are the minimum, the mean, and the maximum relative deviation.

S29 List of band gap values

Table S4: Average band gap values from cited references in eV. The bold printed ones are used for the evaluation in the main text.

Compound	Direct	Indirect	Compound	Direct	Indirect
$CuFe_2O_4$	1.50[8] **1.95**[9,10]	1.30[11,12] 1.95(i)[10]	CuO	1.50[13,14] **3.47**[15–17]	1.36[15–17]
$CuGa_2O_4$	**4.45**[18,19]	–	Cu_2O	**2.23**[13,20]	–
Fe_3O_4	**2.80**[21–23]	2.06[21,23]	$CuFeO_2$	1.12[24,25] **2.08**[25–28] 3.15[29,30]	0.78[24] 1.15[26–28] 1.63[29]
$FeGa_2O_4$	**2.45**[31]	–	$CuGaO_2$	2.48[32] **3.53**[33,34]	1.40[32]

S30 Simulated bandgap map

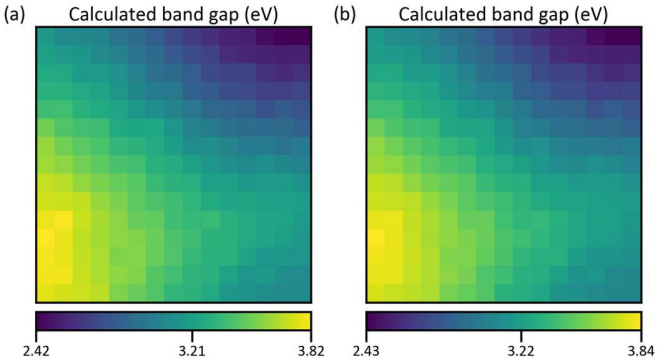

Fig. S37 Calculated direct band gap map as described in the main text, (a) with considering all structures in the crystal structure evaluation and (b) without considering delafossite. The values of the colour bar are the minimum, the mean, and the maximum band gap energy.

S31 Correlation matrix

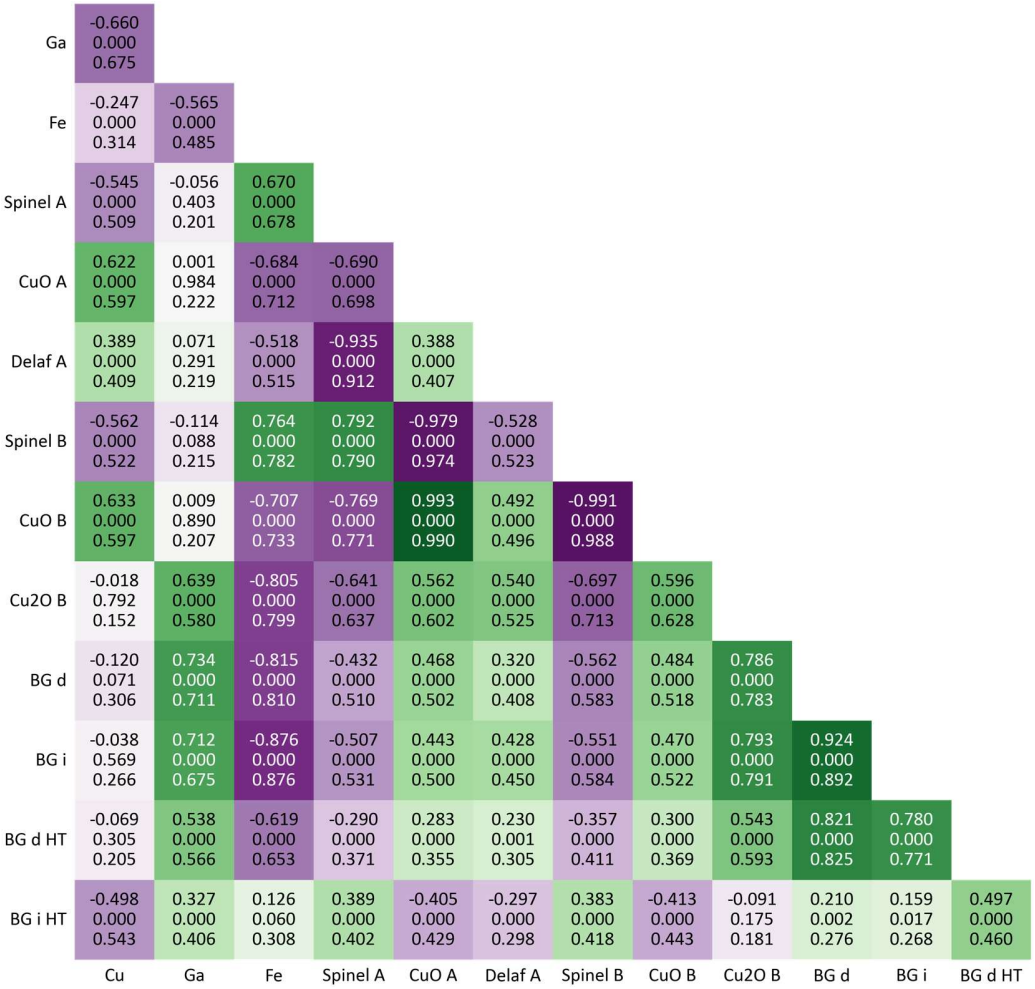

Fig. S38 Correlation matrix for the relationships between the composition, i.e., "Cu", "Ga", and "Fe" for the Cu, Ga, and Fe mole fractions from Fig. 4 b (main text), the crystal structure, i.e., "Spinel", "CuO", "Delaf.", and "Cu2O" for the relative amounts of spinel, CuO, delafossite, and Cu_2O from Fig. 6 (main text), and "BG d" and "BG i" for the direct and indirect band gap energies from Fig. 8 (main text). The suffixes "A" and "B" after crystal structure names refer to the two evaluation results in Fig. 6 a and b (main text), respectively. The "HT" after the band gap name indicates the heat-treated (annealed) film, i.e., Fig. 8 b (main text). The three values in each cell are from top to bottom: (1) linear correlation coefficient, (2) associated p-value, and (3) distance correlation coefficient. The colouring corresponds to the linear correlation coefficient with more saturated green and violet cells for higher positive and negative values, respectively.

S32 References

1 N. W. M. Ritchie, *Microscopy and Microanalysis*, 2005, **11**, 1290–1291.
2 N. W. M. Ritchie, *Microscopy and Microanalysis*, 2009, **15**, 454–468.
3 Octane Elect EDS/EDX System | EDAX, https://www.edax.com/products/eds/www.edax.com/products/eds/octane-elect-eds-system, (accessed 18 January 2023).
4 Patented C-Series Low Energy X-Ray Windows – Amptek – X-Ray Detectors and Electronics, https://www.amptek.com/products/x-ray-detectors/fastsdd-x-ray-detectors-for-xrf-eds/c-series-low-energy-x-ray-windows, (accessed 18 January 2023).
5 2015.
6 L. Filipovic, S. Selberherr, G. C. Mutinati, E. Brunet, S. Steinhauer, A. Köck, J. Teva, J. Kraft, J. Siegert and F. Schrank, *Microelectronic Engineering*, 2014, **117**, 57–66.
7 G. D. Cody, T. Tiedje, B. Abeles, B. Brooks and Y. Goldstein, *Phys. Rev. Lett.*, 1981, **47**, 1480–1483.
8 T. P. Oliveira, S. F. Rodrigues, G. N. Marques, R. C. Viana Costa, C. G. Garçone Lopes, C. Aranas, A. Rojas, J. H. Gomes Rangel and M. M. Oliveira, *Catalysts*, 2022, **12**, 623.
9 K. Shetty, L. Renuka, H. P. Nagaswarupa, H. Nagabhushana, K. S. Anantharaju, D. Rangappa, S. C. Prashantha and K. Ashwini, *Materials Today: Proceedings*, 2017, **4**, 11806–11815.

10 S. Park, J. H. Baek, L. Zhang, J. M. Lee, K. H. Stone, I. S. Cho, J. Guo, H. S. Jung and X. Zheng, *ACS Sustainable Chem. Eng.*, 2019, **7**, 5867–5874.
11 M. M. R. Khan, M. R. Uddin, H. Abdullah, K. M. R. Karim, A. Yousuf, C. K. Cheng and H. R. Ong, , DOI:10.5281/zenodo.1126852.
12 K. Md. Rezaul Karim, M. Tarek, H. R. Ong, H. Abdullah, A. Yousuf, C. K. Cheng and Md. M. R. Khan, *Ind. Eng. Chem. Res.*, 2019, **58**, 563–572.
13 D. Gupta, S. R. Meher, N. Illyaskutty and Z. C. Alex, *Journal of Alloys and Compounds*, 2018, **743**, 737–745.
14 L. Xu, G. Zheng, S. Pei and J. Wang, *Optik*, 2018, **158**, 382–390.
15 F. P. Koffyberg and F. A. Benko, *Journal of Applied Physics*, 1982, **53**, 1173–1177.
16 S. Rehman, A. Mumtaz and S. K. Hasanain, *J Nanopart Res*, 2011, **13**, 2497–2507.
17 M. H. Babu, J. Podder, B. C. Dev and M. Sharmin, *Surfaces and Interfaces*, 2020, **19**, 100459.
18 H. Wei, Z. Chen, Z. Wu, W. Cui, Y. Huang and W. Tang, *AIP Advances*, 2017, **7**, 115216.
19 A. K. Saikumar, S. Sundaresh, S. D. Nehate and K. B. Sundaram, *Coatings*, 2021, **11**, 921.
20 C. Kittel, P. McEuen and P. McEuen, *Introduction to solid state physics*, Wiley New York, 1996, vol. 8.
21 H. El Ghandoor, H. Zidan, M. Khalil and M. I. M. Ismail, *International Journal of Electrochemical Science*.
22 A. Radoń, A. Drygała, Ł. Hawełek and D. Łukowiec, *Materials Characterization*, 2017, **131**, 148–156.
23 P. M. Kouotou, A. E. Kasmi, L.-N. Wu, M. Waqas and Z.-Y. Tian, *Journal of the Taiwan Institute of Chemical Engineers*, 2018, **93**, 427–435.
24 Q.-L. Liu, Z.-Y. Zhao, R.-D. Zhao and J.-H. Yi, *Journal of Alloys and Compounds*, 2020, **819**, 153032.
25 S. Vojkovic, J. Fernandez, S. Elgueta, F. E. Vega, S. D. Rojas, R. A. Wheatley, B. Seifert, S. Wallentowitz and A. L. Cabrera, *SN Appl. Sci.*, 2019, **1**, 1322.
26 F. A. Benko and F. P. Koffyberg, *Journal of Physics and Chemistry of Solids*, 1987, **48**, 431–434.
27 K. P. Ong, K. Bai, P. Blaha and P. Wu, *Chem. Mater.*, 2007, **19**, 634–640.
28 Z. Deng, X. Fang, S. Wu, Y. Zhao, W. Dong, J. Shao and S. Wang, *Journal of Alloys and Compounds*, 2013, **577**, 658–662.
29 H.-Y. Chen and J.-H. Wu, *Applied Surface Science*, 2012, **258**, 4844–4847.
30 A. Shah and A. Azam, 2018, vol. 1942, p. 120006.
31 M. M. Can, Y. Akbaba and S. Kaneko, *Coatings*, 2022, **12**, 423.
32 Q.-M. Zhao, Z.-Y. Zhao, Q.-L. Liu, G.-Y. Yao and X.-D. Dong, *J. Phys. D: Appl. Phys.*, 2020, **53**, 135102.
33 K. Ueda, T. Hase, H. Yanagi, H. Kawazoe, H. Hosono, H. Ohta, M. Orita and M. Hirano, *Journal of Applied Physics*, 2001, **89**, 1790.
34 R.-S. Yu and Y.-C. Lee, *Thin Solid Films*, 2018, **646**, 143–149.